

## Article

# Feasibility Study of Multi-Wavelength Differential Absorption LIDAR for CO<sub>2</sub> Monitoring

Chengzhi Xiang <sup>1</sup>, Xin Ma <sup>1,2</sup>, Ailin Liang <sup>1</sup>, Ge Han <sup>3</sup>, Wei Gong <sup>1,2,\*</sup> and Fa Yan <sup>4</sup>

<sup>1</sup> State Key Laboratory of Information Engineering in Surveying, Mapping and Remote Sensing, Wuhan University, Wuhan 430079, China; cxiang@whu.edu.cn (C.X.); maxinwhu@gmail.com (X.M.); ireneliang@whu.edu.cn (A.L.)

<sup>2</sup> Collaborative Innovation Center for Geospatial Technology, Wuhan 430079, China

<sup>3</sup> International School of Software, Wuhan University, Wuhan 430079, China; udhan@whu.edu.cn

<sup>4</sup> Huawei Technologies Co., Ltd., Shenzhen 518129, China; yanfa0226@163.com

\* Correspondence: weigong@whu.edu.cn; Tel.: +86-27-6877-8318

Academic Editor: Robert W. Talbot

Received: 17 May 2016; Accepted: 27 June 2016; Published: 30 June 2016

**Abstract:** To obtain a better understanding of carbon cycle and accurate climate prediction models, highly accurate and temporal resolution observation of atmospheric CO<sub>2</sub> is necessary. Differential absorption LIDAR (DIAL) remote sensing is a promising technology to detect atmospheric CO<sub>2</sub>. However, the traditional DIAL system is the dual-wavelength DIAL (DW-DIAL), which has strict requirements for wavelength accuracy and stability. Moreover, for on-line and off-line wavelengths, the system's optical efficiency and the change of atmospheric parameters are assumed to be the same in the DW-DIAL system. This assumption inevitably produces measurement errors, especially under rapid aerosol changes. In this study, a multi-wavelength DIAL (MW-DIAL) is proposed to map atmospheric CO<sub>2</sub> concentration. The MW-DIAL conducts inversion with one on-line and multiple off-line wavelengths. Multiple concentrations of CO<sub>2</sub> are then obtained through difference processing between the single on-line and each of the off-line wavelengths. In addition, the least square method is adopted to optimize inversion results. Consequently, the inversion concentration of CO<sub>2</sub> in the MW-DIAL system is found to be the weighted average of the multiple concentrations. Simulation analysis and laboratory experiments were conducted to evaluate the inversion precision of MW-DIAL. For comparison, traditional DW-DIAL simulations were also conducted. Simulation analysis demonstrated that, given the drifting wavelengths of the laser, the detection accuracy of CO<sub>2</sub> when using MW-DIAL is higher than that when using DW-DIAL, especially when the drift is large. A laboratory experiment was also performed to verify the simulation analysis.

**Keywords:** feasibility study; multi-wavelength; differential absorption LIDAR; CO<sub>2</sub> monitoring

## 1. Introduction

Global warming is now considered indisputable, a fact that has been further confirmed by the fifth working report of the International Panel of Climate Change (IPCC). Greenhouse gas emissions and other human-driven factors have been the main causes of global warming since the mid-20th century [1–3]. The concentration of atmospheric CO<sub>2</sub>, which is one of the most important greenhouse gases, has increased by more than 100 parts per million (ppm) from approximately 280 to 400 ppm since the Industrial Revolution [4]. However, previous studies demonstrate that the global carbon cycle cannot be predicted exactly by existing atmospheric models [5–7]. The natural geographic distribution and temporal variability of CO<sub>2</sub> sources and sinks remain largely uncertain, especially for urbanized areas where high-level sources are located [8,9]. In this case, precise monitoring of atmospheric CO<sub>2</sub> concentration is necessary.

Differential absorption LIDAR (DIAL) has been widely used to detect atmospheric CO<sub>2</sub> [10–13]. This technique not only measures the columnar CO<sub>2</sub> but also provides vertical profiles of CO<sub>2</sub> concentration distribution. Traditional DIAL (DW-DIAL) is a dual (i.e., on-line and off-line) wavelength system that can perform high-precision detection. However, the DW-DIAL system is complex and has high technical requirements for measuring atmospheric CO<sub>2</sub>. A strict wavelength stabilization system is required; otherwise, differential detection becomes erroneous.

In this study, a ground-based multi-wavelength DIAL (MW-DIAL) is proposed for atmospheric CO<sub>2</sub> monitoring. The MW-DIAL maps CO<sub>2</sub> concentration with a single on-line and multiple off-line wavelengths. All of these wavelengths are obtained through multi-wavelength scanning, which involves continuous sampling across the CO<sub>2</sub> absorption line with an appropriate number of points and range of widths. After sampling at multiple wavelengths across the absorption line, the complete absorption line of CO<sub>2</sub>—including the absorption peak and valley—can be obtained through curve fitting. The position of different wavelengths can then be obtained at the absorption line. This prevents their locations from being strictly locked, especially that of the on-line wavelength. Sampling at multiple wavelengths across the absorption line is a unique method used in CO<sub>2</sub> detection and has been adopted by Abshire et al. and Refaat et al. [14–16]. This study primarily analyzes the feasibility of MW-DIAL for CO<sub>2</sub> monitoring from the inversion algorithm. In the study, multiple concentrations of CO<sub>2</sub> are obtained by means of the difference processing between the on-line and each off-line wavelength. In addition, the least square method is adopted to optimize inversion results. The inversion concentration of CO<sub>2</sub> is identified as the weighted average of the multiple concentrations, and the weights are determined based on the difference of the absorption cross section of on-line and off-line wavelengths.

The remainder of this study is organized as follows. The principle and the laser transmitter of MW-DIAL are described in Section 2. Relevant information about the inversion algorithm is introduced in Section 3. Simulation analysis and laboratory experiments on two systems (MW-DIAL and DW-DIAL) are discussed in Sections 4 and 5, respectively. Section 6 summarizes the most important findings and describes the limitations of this study.

## 2. Principle and Method

DIAL is an attractive method for detecting CO<sub>2</sub>, water vapor, temperature, ozone, and aerosols [17,18]. In the DW-DIAL system, two laser pulses with similar wavelengths are transmitted. One laser is located at the absorption peak of the detected component to obtain the maximum absorption, called the on-line wavelength ( $\lambda_{\text{on}}$ ). The other laser is near the valley of absorption, which causes the absorption to be as small as possible, called the off-line wavelength ( $\lambda_{\text{off}}$ ).

The LIDAR equations of the on-line and off-line wavelengths can be written as [19,20]:

$$P(\lambda, r) = \frac{K \cdot P_0 \cdot A \cdot c \cdot \frac{\tau}{2}}{r^2} \cdot \beta(\lambda, r) \cdot \exp \left\{ -2 \cdot \int_0^r [\alpha_0(\lambda, r) + N_g(r) \cdot \sigma_g(\lambda)] dr \right\} \quad (1)$$

where  $r$  is the detection range,  $P(\lambda, r)$  is the received power of range  $r$  ( $\lambda$  can be both on-line and off-line wavelengths),  $P_0$  is the laser output power,  $K$  is the calibration constant for the LIDAR,  $A$  is the light area of the receiving telescope,  $c$  is the speed of light,  $\tau$  is the laser pulse duration,  $\beta(\lambda, r)$  is the backscatter coefficient of the atmosphere,  $\alpha_0(\lambda, r)$  is the extinction coefficient of the atmosphere (excluding the trace gas under study),  $N_g(r)$  is the number of trace gas density, and  $\sigma_g(r)$  is the absorption cross section of the trace gas.

When the laser wavelength range is small and the time frame is short, several atmospheric parameters change slightly with the wavelength, which can be regarded as constants in the DIAL system. Furthermore, closely neighboring spectral lines are often adopted for atmospheric CO<sub>2</sub> measurements. Consequently, a slight change in wavelength implies a negligible change in the target reflectivity, system efficiency, and other factors such as atmospheric attenuation [21–24].

In the DIAL system, Equation (1) with on-line wavelength is divided by that with off-line wavelength. The number density of range-resolved atmospheric CO<sub>2</sub> can then be derived from the following equation:

$$N_g(r) = \frac{1}{2 \cdot \Delta r \cdot [\sigma_g(\lambda_{on}) - \sigma_g(\lambda_{off})]} \ln \left[ \frac{P(\lambda_{off}, r_2) \cdot P(\lambda_{on}, r_1)}{P(\lambda_{on}, r_2) \cdot P(\lambda_{off}, r_1)} \right] \quad (2)$$

where  $r_1$  and  $r_2$  are the beginning and end of the integration interval, respectively, and  $\Delta r = r_2 - r_1$  is the range resolution.

In addition, the concentration of CO<sub>2</sub> (unit: ppm) can be obtained using the following equation with the number density.

$$C = N \cdot \frac{R \cdot T}{N_A \cdot P} \times 10^6 \quad (3)$$

where  $N_A$  is the Avogadro constant of approximately  $6.022 \times 10^{23} \text{ mol}^{-1}$ ;  $P$ ,  $T$  are the pressure and temperature of gas, respectively;  $R$  is the ideal gas constant of approximately  $8.314 \text{ J}/(\text{K} \cdot \text{mol})$ .

In addition, Equation (2) could be expressed as the following equation by optical depth (OD) and differential absorption optical depth (DAOD).

$$N_g(r) = \frac{DAOD}{2 \cdot \Delta r \cdot \Delta \sigma} = \frac{OD(on) - OD(off)}{2 \cdot \Delta r \cdot [\sigma_g(\lambda_{on}) - \sigma_g(\lambda_{off})]} \quad (4)$$

The principle and method of detection of MW-DIAL are similar to those of the DW-DIAL. The difference lies in the transmitted system and inversion algorithm. The transmitted lasers of the DW-DIAL consist of two wavelengths, whereas those of MW-DIAL consist of multiple wavelengths. The case is the same for the inversion algorithm. Figure 1 is a block diagram of an MW-DIAL system. The inversion algorithm is introduced in Section 3.

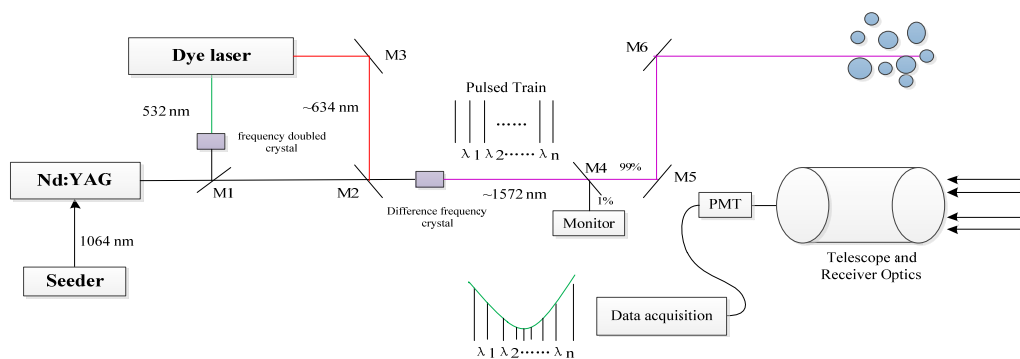


**Figure 1.** Block of the multi-wavelength differential absorption LIDAR (MW-DIAL) system. M1 is a semi-transmitting reflecting mirror; M2 and M4 are one-sided antireflection-coated glass devices; M3, M5, and M6 are reflecting mirrors.

In the MW-DIAL system as shown in Figure 1, a tunable dye laser is used to generate different wavelengths. The target wavelength is generated through difference frequency mixing between the fundamentals of the Nd:YAG laser (1064 nm) and the dye laser (634 nm), which is pumped by the second harmonic of the Nd:YAG (532 nm). Consequently, the wavelength of the output laser can be changed by tuning the dye laser, whose wavelength is changed by a stepper motor [25]. The different transmitted wavelengths are then vertically launched into the air. A receiving system is used to receive the echo signals for both on-line and off-line wavelengths. After passing the corresponding filter and small aperture, the received optical signals are then transferred to an infrared photomultiplier tube for amplification and conversion into electricity. The signal is shown in an oscilloscope in real time

and can be collected using a data-collecting card. Finally, the vertical profile of atmospheric CO<sub>2</sub> concentration is derived by calculating the data using the inversion algorithm.

The single on-line and multiple off-line wavelengths are obtained through multi-wavelength scanning. This involves continuous sampling across the CO<sub>2</sub> absorption line with an appropriate number of points and range of widths. This approach is flexible, and the number of different wavelengths for measuring the CO<sub>2</sub> line shape is variable. Sampling at multiple wavelengths across the absorption line also enables solving for the wavelength offsets by means of a curve fitting process.

### 3. Inversion Algorithm

The inversion algorithm of MW-DIAL is similar to that of DW-DIAL. Supposing an on-line wavelength and  $m$  off-line wavelengths are transmitted, the number of echo signals that can be obtained is  $m$ . The LIDAR equations of different wavelengths can be written as:

$$P(\lambda_t, r) = \frac{K(\lambda_t) \cdot P_0 \cdot A \cdot c \cdot \frac{\pi}{2}}{r^2} \cdot \beta(\lambda_t, r) \cdot \exp \left\{ -2 \cdot \int_0^r [\alpha_0(\lambda_t, r) + N_{\text{CO}_2}(r) \cdot \sigma_{\text{CO}_2}(\lambda_t)] dr \right\}, (t = \text{on}, 1, 2, \dots, m) \quad (5)$$

Difference processing is conducted between the single on-line and each off-line wavelength.  $M$  differential inverse equations are obtained, as expressed in the following equation.

$$\begin{cases} N_{\text{CO}_2}(r) = \frac{1}{2 \cdot \Delta r \cdot [\sigma_{\text{CO}_2}(\lambda_{\text{on}}, r) - \sigma_{\text{CO}_2}(\lambda_1, r)]} \ln \left[ \frac{P(\lambda_1, r_2) \cdot P(\lambda_{\text{on}}, r_1)}{P(\lambda_{\text{on}}, r_2) \cdot P(\lambda_1, r_1)} \right] \\ N_{\text{CO}_2}(r) = \frac{1}{2 \cdot \Delta r \cdot [\sigma_{\text{CO}_2}(\lambda_{\text{on}}, r) - \sigma_{\text{CO}_2}(\lambda_2, r)]} \ln \left[ \frac{P(\lambda_2, r_2) \cdot P(\lambda_{\text{on}}, r_1)}{P(\lambda_{\text{on}}, r_2) \cdot P(\lambda_2, r_1)} \right] \\ \vdots \\ N_{\text{CO}_2}(r) = \frac{1}{2 \cdot \Delta r \cdot [\sigma_{\text{CO}_2}(\lambda_{\text{on}}, r) - \sigma_{\text{CO}_2}(\lambda_m, r)]} \ln \left[ \frac{P(\lambda_m, r_2) \cdot P(\lambda_{\text{on}}, r_1)}{P(\lambda_{\text{on}}, r_2) \cdot P(\lambda_m, r_1)} \right] \end{cases} \quad (6)$$

The least square method [26,27] is adopted to address the residual series and to optimize inversion results. Echo signals are considered to be observed values, the number density of CO<sub>2</sub> molecule ( $N_{\text{CO}_2}(r)$ ) is regarded as a parameter, the absorption cross section is the coefficient, and the random error of the echo signal is added. Thus, the following equation can be obtained:

$$\begin{cases} \ln \left[ \frac{P(\lambda_1, r_2) \cdot P(\lambda_{\text{on}}, r_1)}{P(\lambda_{\text{on}}, r_2) \cdot P(\lambda_1, r_1)} \right] + \varepsilon_2 = 2 \cdot \Delta r \cdot [\sigma_{\text{CO}_2}(\lambda_{\text{on}}, r) - \sigma_{\text{CO}_2}(\lambda_1, r)] \cdot N_{\text{CO}_2}(r) \\ \ln \left[ \frac{P(\lambda_2, r_2) \cdot P(\lambda_{\text{on}}, r_1)}{P(\lambda_{\text{on}}, r_2) \cdot P(\lambda_2, r_1)} \right] + \varepsilon_2 = 2 \cdot \Delta r \cdot [\sigma_{\text{CO}_2}(\lambda_{\text{on}}, r) - \sigma_{\text{CO}_2}(\lambda_2, r)] \cdot N_{\text{CO}_2}(r) \\ \vdots \\ \ln \left[ \frac{P(\lambda_m, r_2) \cdot P(\lambda_{\text{on}}, r_1)}{P(\lambda_{\text{on}}, r_2) \cdot P(\lambda_m, r_1)} \right] + \varepsilon_m = 2 \cdot \Delta r \cdot [\sigma_{\text{CO}_2}(\lambda_{\text{on}}, r) - \sigma_{\text{CO}_2}(\lambda_m, r)] \cdot N_{\text{CO}_2}(r) \end{cases} \quad (7)$$

Supposing that

$$B = [B_1 \ B_2 \ \dots \ B_m]^T = \begin{bmatrix} 2 \cdot \Delta r \cdot [\sigma_{\text{CO}_2}(\lambda_{\text{on}}, r) - \sigma_{\text{CO}_2}(\lambda_1, r)] \\ 2 \cdot \Delta r \cdot [\sigma_{\text{CO}_2}(\lambda_{\text{on}}, r) - \sigma_{\text{CO}_2}(\lambda_2, r)] \\ \vdots \\ 2 \cdot \Delta r \cdot [\sigma_{\text{CO}_2}(\lambda_{\text{on}}, r) - \sigma_{\text{CO}_2}(\lambda_m, r)] \end{bmatrix}$$

$$L = [L_1 \ L_2 \ \dots \ L_m]^T = \begin{bmatrix} \ln \left[ \frac{P(\lambda_1, r_2) \cdot P(\lambda_{\text{on}}, r_1)}{P(\lambda_{\text{on}}, r_2) \cdot P(\lambda_1, r_1)} \right] \\ \ln \left[ \frac{P(\lambda_2, r_2) \cdot P(\lambda_{\text{on}}, r_1)}{P(\lambda_{\text{on}}, r_2) \cdot P(\lambda_2, r_1)} \right] \\ \vdots \\ \ln \left[ \frac{P(\lambda_m, r_2) \cdot P(\lambda_{\text{on}}, r_1)}{P(\lambda_{\text{on}}, r_2) \cdot P(\lambda_m, r_1)} \right] \end{bmatrix}, V = \begin{bmatrix} \varepsilon_1 \\ \varepsilon_2 \\ \vdots \\ \varepsilon_m \end{bmatrix}$$

Then,

$$V = B \cdot N_{\text{CO}_2}(R) - L \quad (8)$$

where  $L$  is an  $m$ -dimensional observation vector,  $B$  is an  $m \times 1$ -dimensional coefficient matrix,  $N_{CO_2}(r)$  is a one-dimensional unknown parameter vector, and  $V$  is a residual vector of observations.

Assuming that the weight matrix of the observation is  $P = \text{diag}[P_1 \ P_2 \ \cdots \ P_m]$ , then  $m$  redundant observation equations are given in Equation (6). According to the criterion of weighted least square estimation, the optimal solution of  $N_{CO_2}(r)$  should meet  $\sum P_i \varepsilon_i^2 = \min$ , which is given as:

$$V^T P V = \min \quad (9)$$

A derivation from the condition is calculated:

$$\frac{\partial V^T P V}{\partial N_{CO_2}(R)} = 2V^T P \frac{\partial V}{\partial N_{CO_2}(R)} = 2V^T P B = 0$$

After the transposition, the following equation is obtained:

$$B^T P V = 0 \quad (10)$$

Merging Equation (8) into Equation (10) obtains:

$$B^T P B \cdot N_{CO_2}(r) - B^T P L = 0 \quad (11)$$

The coefficient matrix ( $B^T P B$ ) is a full rank. In other words,  $R(B^T P B) = m$ .  $N_{CO_2}(r)$  then has a unique solution.

$$N_{CO_2}(r) = (B^T P B)^{-1} \cdot B^T P L \quad (12)$$

The weight matrix ( $P$ ) can be defined simply as a unit matrix and can be determined based on the signal to noise ratio (SNR) of the signal as a number matrix. Supposing that  $P$  is a unit matrix, Equation (12) can be expressed as:

$$N_{CO_2}(r) = (B^T B)^{-1} \cdot B^T L \quad (13)$$

Given that  $B^T L = B_1 L_1 + B_2 L_2 + \cdots + B_m L_m$ ,  $N_i(R) = \frac{1}{B_i} L_i$  ( $i = 1, 2, \cdots, m$ ), Equation (12) can be written as

$$N_{CO_2}(R) = \frac{B_1^2}{B_1^2 + B_2^2 + \cdots + B_m^2} \cdot N_1(R) + \frac{B_2^2}{B_1^2 + B_2^2 + \cdots + B_m^2} \cdot N_2(R) + \cdots + \frac{B_m^2}{B_1^2 + B_2^2 + \cdots + B_m^2} \cdot N_m(R) \quad (14)$$

As shown in Equation (14), when the weight matrix ( $P$ ) is defined as a unit matrix, the inversion concentration through the MW-DIAL is represented as the weighted averages of the multiple concentrations detected by the DW-DIAL. The weights are determined by the difference of the absorption cross section of the dual wavelengths.

#### 4. Simulation Analysis

To evaluate the feasibility and accuracy of MW-DIAL for atmospheric  $CO_2$  detection, we conducted a series of simulated experiments. Most spectroscopic parameters of  $CO_2$  lines for the simulation analysis were obtained from Predoi-Cross et al. [28] and HITRAN 2012 [29]. The spectroscopic parameters of the absorption lines of  $H_2O$  were obtained from HITEMP 2010 [30,31]. According to the HITRAN 2012 molecular spectroscopic database, six absorption lines in the range of the 30012–00001 carbon-dioxide band were studied because their intensities were evidently higher than those of others. The spectroscopic parameters of the absorption lines of  $CO_2$ , which are marked as C1–C6 (namely, R10–R20), and those of  $H_2O$  in this range are listed in Table 1. The absorption lines are also presented in Figure 2, with the absorption cross sections of the  $H_2O$  and  $CO_2$  molecules at 101325 Pa and 296 K calculated using the Voigt profile. In spectroscopy, the Voigt profile is a line

profile that results from the convolution of two broadening mechanisms. One of the broadening mechanisms produces a Gaussian profile as a result of the Doppler broadening; the other produces a Lorentz profile. Because of its physical implications, the Voigt function is superior to other functions for obtaining the absorption line of CO<sub>2</sub> [25]. The H<sub>2</sub>O curve, which marks the right axis, is on a log scale, given that the intensities of the lines are much smaller than those of CO<sub>2</sub>. H1–H13 were not labeled because our concern was their effects on CO<sub>2</sub>. In selecting the operating wavelength, we had to consider many factors, such as low temperature sensitivity and low interference from other molecules. Previous studies showed that H<sub>2</sub>O is the most critical interference molecule in the absorption spectroscopy of CO<sub>2</sub> [31,32]. As shown in Figure 2, R10, R12, and R20 are inappropriate because they are considerably affected by interferences from H<sub>2</sub>O. R16 is the most appropriate because the intensity of this peak is the strongest, and the influence of H<sub>2</sub>O in this band is less than that in R14 and R18. Consequently, less noise is generated, and the differential optical depth is the largest. Thus, R16 has the highest SNR in this range and is recommended for measuring atmospheric CO<sub>2</sub> using DIAL at 1572 nm.

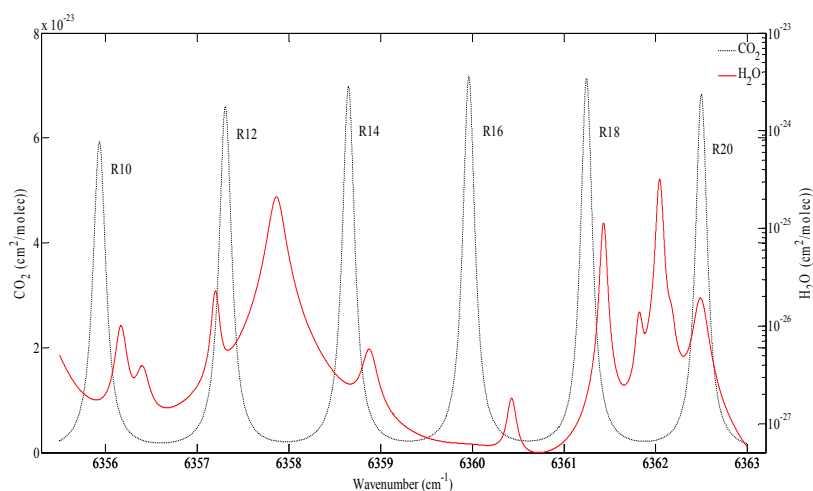


**Figure 2.** Calculated absorption cross sections of CO<sub>2</sub> and H<sub>2</sub>O based on HITRAN 2012 and HITEMP 2010.

**Table 1.** Spectroscopic parameters of CO<sub>2</sub> and H<sub>2</sub>O involved in the simulation analysis.

Abb.	Position	Intensity	bL (Air)	E''	n	δ° (Air)	δ' (Air)	P(pa)	T(K)
C1	6355.939	$1.534 \times 10^{-23}$	0.080	42.92	0.696	$-4.59 \times 10^{-3}$	$-5.7 \times 10^{-5}$	101325	296
C2	6357.312	$1.661 \times 10^{-23}$	0.078	60.87	0.695	$-4.30 \times 10^{-3}$	$-7.0 \times 10^{-5}$	101325	296
C3	6358.654	$1.730 \times 10^{-23}$	0.077	81.94	0.680	$-4.92 \times 10^{-3}$	$-6.3 \times 10^{-5}$	101325	296
C4	6359.967	$1.741 \times 10^{-23}$	0.075	106.13	0.672	$-4.98 \times 10^{-3}$	$-8.3 \times 10^{-5}$	101325	296
C5	6361.250	$1.703 \times 10^{-23}$	0.074	133.44	0.653	$-5.60 \times 10^{-3}$	$-6.8 \times 10^{-5}$	101325	296
C6	6362.504	$1.621 \times 10^{-23}$	0.073	163.87	0.693	$-6.45 \times 10^{-3}$	$-6.5 \times 10^{-5}$	101325	296
H1	6361.442	$8.875 \times 10^{-27}$	0.017	1327.12	-0.06	-0.0120	—	101325	296
H2	6356.177	$1.469 \times 10^{-27}$	0.048	1079.08	0.45	-0.0074	—	101325	296
H3	6355.156	$3.130 \times 10^{-26}$	0.060	586.48	0.34	-0.0060	—	101325	296
H4	6356.415	$5.440 \times 10^{-28}$	0.065	2919.63	0.44	-0.0127	—	101325	296
H5	6357.208	$5.550 \times 10^{-28}$	0.030	2254.28	0.01	-0.0090	—	101325	296
H6	6357.209	$1.660 \times 10^{-27}$	0.029	2254.28	0.01	-0.0094	—	101325	296
H7	6357.881	$1.760 \times 10^{-26}$	0.076	1899.01	0.59	-0.0195	—	101325	296
H8	6357.881	$3.430 \times 10^{-26}$	0.075	610.34	0.58	-0.0160	—	101325	296
H9	6358.894	$1.090 \times 10^{-27}$	0.074	2764.70	0.53	-0.0175	—	101325	296
H10	6361.838	$1.020 \times 10^{-27}$	0.025	2972.83	0.09	-0.0171	—	101325	296
H11	6362.055	$2.550 \times 10^{-26}$	0.018	1327.11	-0.06	-0.0120	—	101325	296
H12	6360.456	$2.070 \times 10^{-28}$	0.041	2927.94	0.37	-0.0273	—	101325	296
H13	6362.486	$4.040 \times 10^{-27}$	0.066	610.11	0.80	0.0020	—	101325	296

Position—Zero pressure line positions in cm<sup>-1</sup>; Intensity—Line intensities in cm/molecule<sup>-1</sup> at 296 K; bL (air)—Air-broadened Lorentz width coefficients in cm<sup>-1</sup>·atm<sup>-1</sup> at 296 K; E''—Lower-state energy in cm<sup>-1</sup>; n—Temperature dependence exponents of air-broadened half-width coefficients (unitless); δ° (air)—Pressure-shift coefficients in cm<sup>-1</sup>·atm<sup>-1</sup> at 296 K; δ' (air)—Temperature-dependent coefficients of air-shift coefficients in cm<sup>-1</sup>·atm<sup>-1</sup>·K<sup>-1</sup>.



#### 4.1. Simulation Analysis of Wavelength Shift

The simulation analysis of wavelength shift was conducted in three parts. The first part concerned theoretical inversion, in which both the parameters of on-line and off-line wavelengths were theoretical values. Results of this inversion were supposed to be 400 ppm, which is marked as  $C_0$  and used as the evaluation criterion for inversion. The logarithm of the energy ratio (i.e., DAOD) of on-line and off-line wavelengths was obtained using Equations (2) and (3). The DAOD was used for inversion in the second and third parts, which were both under the conditions of lasers with shifting wavelengths. The methods of inversion for the last two parts were DW-DIAL and MW-DIAL, respectively. The inversion results are marked as  $C_1$  and  $C_2$ . Finally,  $C_0$ ,  $C_1$ , and  $C_2$  were compared to obtain the inversion accuracy of  $\text{CO}_2$  using the different methods.

##### 4.1.1. Part 1

As shown in Figure 3, in the section of the on-line and off-line wavelengths in the region of R16, the on-line wavelength could be easily obtained because only one absorption peak of  $\text{CO}_2$  was observed in the region of R16, which is marked as 2. The theoretical wavelength of point 2 was  $6359.962 \text{ cm}^{-1}$ . However, two absorption valleys of  $\text{CO}_2$  were found on both sides of the on-line wavelength, which are marked as 1 and 3, respectively. According to the spectroscopic parameters of the  $\text{CO}_2$  lines from HITRAN 2012, the intensity of Point 1 was lower than that of Point 3, but Point 1 was largely affected by the water vapor. The intensity of water vapor at Point 1 was approximately  $8.9162 \times 10^{-28}$  whereas that at Point 3 was  $5.4435 \times 10^{-28}$ . Consequently, Point 3 was considered to be the position of the off-line wavelength, and its wavelength was  $6360.609 \text{ cm}^{-1}$ .

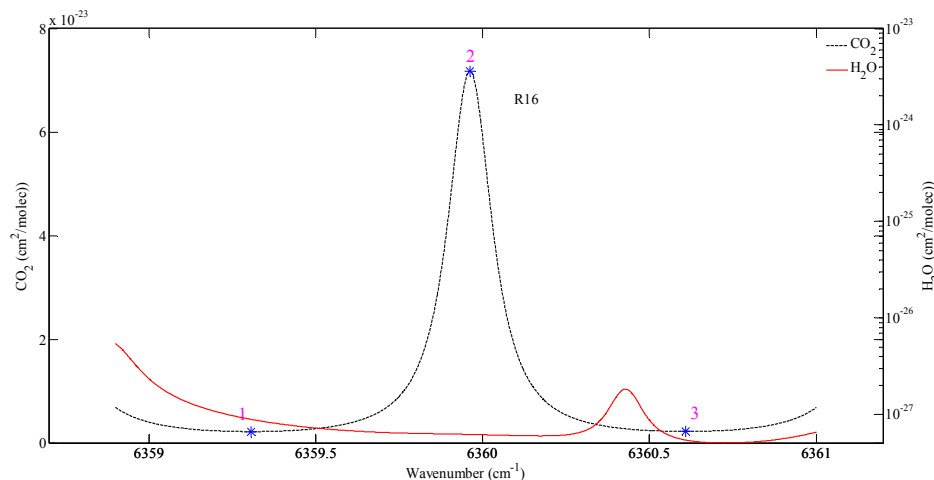


**Figure 3.** Selections of the on-line and off-line wavelengths in the region of R16 for the dual-wavelength DIAL (DW-DIAL). The black dotted and red lines are the absorption lines of  $\text{CO}_2$  and  $\text{H}_2\text{O}$ , respectively.

According to Section 2, the DAOD of the on-line and off-line wavelengths could be easily obtained through the DW-DIAL: supposing that  $r_1 = 0$ ,  $r_2 = 50$ ,  $P(\lambda_{\text{on}}, r_1) = P(\lambda_{\text{off}}, r_1) = 4 \text{ mJ}$ ,  $C_0 = 400 \text{ ppm}$ . In addition,  $\sigma_g(\lambda_{\text{on}})$  and  $\sigma_g(\lambda_{\text{off}})$  could be obtained from HITRAN 2012, which were  $7.1785 \times 10^{-23}$  and  $2.2250 \times 10^{-24} \text{ cm}^2$ , respectively. Then,  $N_0 = 1.0747 \times 10^{22}$ , and  $\text{DAOD} = \ln \frac{P(\lambda_{\text{off}}, r_2)}{P(\lambda_{\text{on}}, r_2)} = 7.476 \times 10^{-3}$  for the on-line and off-line wavelengths of DW-DIAL based on Equations (2) and (3).

In the system of MW-DIAL, the number and position of multiple wavelengths were various and could be adjusted according to the situation. The general concept here is that all points are distributed on both sides of the absorption peak. Points close to the absorption peak are relatively dense, whereas those away from the absorption peak are sparse. In this study, 11 points were selected for the simulated experiments using MW-DIAL. Their positions are shown in Figure 4.

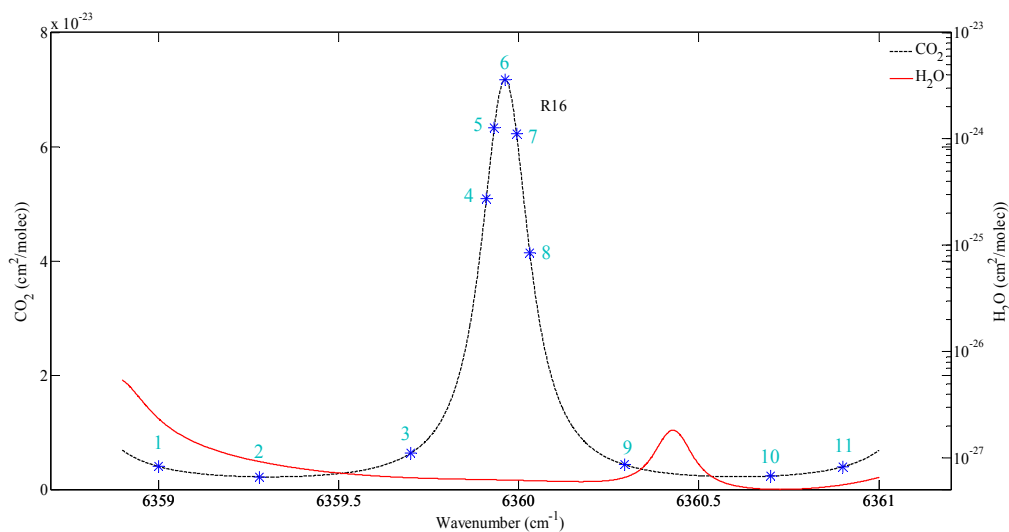


**Figure 4.** Selections of the multiple wavelengths in the region of R16 for the MW-DIAL. The black dotted and red lines are the absorption lines of CO<sub>2</sub> and H<sub>2</sub>O, respectively.

The calculation of DAOD for MW-DIAL is similar to that for DW-DIAL. In this study, the points distributed on both sides of the absorption peak were regarded as the off-line wavelengths and used in the difference processing with the on-line wavelength. DAODs of the on-line and each off-line wavelength were obtained according to Equations (2) and (3), which are listed in Table 2.

**Table 2.** Parameters of the selected points in the MW-DIAL.

$\lambda$ (cm <sup>-1</sup> )	$\sigma$ (cm <sup>2</sup> )	DAOD
6359.000	$4.0309 \times 10^{-24}$	$7.282 \times 10^{-3}$
6359.280	$2.2087 \times 10^{-24}$	$7.478 \times 10^{-3}$
6359.700	$6.3319 \times 10^{-24}$	$7.035 \times 10^{-3}$
6359.910	$5.0866 \times 10^{-23}$	$2.248 \times 10^{-3}$
6359.932	$6.3286 \times 10^{-23}$	$9.135 \times 10^{-4}$
6359.962	$7.1785 \times 10^{-23}$	0.0000
6359.994	$6.2279 \times 10^{-23}$	$1.022 \times 10^{-3}$
6360.031	$4.1391 \times 10^{-23}$	$3.267 \times 10^{-3}$
6360.295	$4.3222 \times 10^{-24}$	$7.251 \times 10^{-3}$
6360.700	$2.3463 \times 10^{-24}$	$7.463 \times 10^{-3}$
6360.900	$3.9719 \times 10^{-24}$	$7.288 \times 10^{-3}$

#### 4.1.2. Part 2

Part 2 involved the analysis of inversion through DW-DIAL under the condition of lasers with shifting wavelengths. Supposing that the shift of on-line and off-line wavelengths was 1 pm, which is approximately  $0.004 \text{ cm}^{-1}$  in the region of R16, the absorption cross sections of on-line and off-line wavelengths became  $\sigma_g(\lambda_{\text{on}}) = 7.1785 \times 10^{-23} \text{ cm}^2$  and  $\sigma_g(\lambda_{\text{off}}) = 2.2250 \times 10^{-24} \text{ cm}^2$  from HITRAN 2012. However, they were still considered to be located at the absorption peak and valley, and their original values were used in the inversion. Accordingly, an error result in the inversion was produced. The inversion errors of different shifts of wavelength in the DW-DIAL are listed in Table 3. The shifts of on-line and off-line wavelengths were 1, 2, 3, 7, and 9 pm, respectively. Note from Table 3 that the inversion error increases rapidly as the shift of on-line and off-line wavelengths increases. In addition, the errors caused by wavelength shift in the left direction are greater than those in the right direction. This is probably because of the difference between the left and right parts of the CO<sub>2</sub> absorption line.



**Table 3.** Inversion error analysis of different shifts of wavelength in the DW-DIAL.

$\Delta\lambda$ (pm)	Direction	$\lambda$ (cm <sup>-1</sup> )		$\sigma$ (cm <sup>2</sup> )		$n$	C (ppm)
		$\lambda$ (on)	$\lambda$ (off)	$\sigma$ (on)	$\sigma$ (off)		
0		6359.962	6360.609	$7.1785 \times 10^{-23}$	$2.2250 \times 10^{-24}$	$1.0747 \times 10^{22}$	400.00
1	R	6359.966	6360.613	$7.1619 \times 10^{-23}$	$2.2252 \times 10^{-24}$	$1.0722 \times 10^{22}$	399.04
	L	6359.958	6360.605	$7.1615 \times 10^{-23}$	$2.2252 \times 10^{-24}$	$1.0721 \times 10^{22}$	399.02
2	R	6359.970	6360.617	$7.1118 \times 10^{-23}$	$2.2259 \times 10^{-24}$	$1.0644 \times 10^{22}$	396.16
	L	6359.954	6360.601	$7.1112 \times 10^{-23}$	$2.2258 \times 10^{-24}$	$1.0643 \times 10^{22}$	396.12
5	R	6359.982	6360.629	$6.7781 \times 10^{-23}$	$2.2307 \times 10^{-24}$	$1.0128 \times 10^{22}$	376.94
	L	6359.942	6360.589	$6.7766 \times 10^{-23}$	$2.2305 \times 10^{-24}$	$1.0126 \times 10^{22}$	376.85
7	R	6359.990	6360.637	$6.4296 \times 10^{-23}$	$2.2362 \times 10^{-24}$	$9.5885 \times 10^{21}$	356.87
	L	6359.934	6360.581	$6.4277 \times 10^{-23}$	$2.2358 \times 10^{-24}$	$9.5856 \times 10^{21}$	356.76
9	R	6359.988	6360.645	$6.0128 \times 10^{-23}$	$2.2436 \times 10^{-24}$	$8.9435 \times 10^{21}$	332.86
	L	6359.926	6360.573	$6.0107 \times 10^{-23}$	$2.2430 \times 10^{-24}$	$8.9402 \times 10^{21}$	332.74

#### 4.1.3. Part 3

Part 3 involved an analysis of inversion through MW-DIAL under the condition of lasers with shifting wavelengths. This analysis processing was similar to that in Part 2. Supposing a shift of on-line and off-line wavelengths occurred in the region of R16, causing a change in the absorption cross sections of multiple wavelengths. However, they were still considered to be located at the original positions, and their original values were used in the inversion. Accordingly, an error in the inversion was produced.

Given the many points that participate in the inversion, all parameters of the points are not listed. For Part 3 of the simulation, a list of only the final inversion results is shown in Table 4.

**Table 4.** Inversion error analysis of different shifts of wavelength in the MW-DIAL.

$\Delta\lambda$ (pm)	0	1	2	5	7	9
C (ppm)	R	399.56	397.83	383.68	364.77	336.42
	L	399.22	397.21	383.14	365.78	340.47

As shown in Tables 3 and 4, given the drifting wavelengths of the laser, the detection accuracy of MW-DIAL for CO<sub>2</sub> was higher than that of DW-DIAL, especially when the drift was large.

#### 4.2. Simulation Analysis of Different SNRs

In addition, we have also analyzed the inversion precision of two methods with echo signal of different SNRs to evaluate the feasibility and accuracy of MW-DIAL for atmospheric CO<sub>2</sub> detection. The simulation analysis of different SNRs was conducted in two parts.

##### 4.2.1. Part 1

For the DW-DIAL, echo signal of on-line and off-line wavelengths with a range of 5 km was simulated for the analysis, which is shown in Figure 5. The initial CO<sub>2</sub> concentration was assumed to be 400 ppm, and the temperature and pressure profiles were obtained by interpolating the sounding data of the temperature and pressure. Compared with the off-line wavelength, the on-line wavelength fell more rapidly due to CO<sub>2</sub> absorption. When dealing with pure signals, DAOD was calculated based on the signal intensity of on-line and off-line wavelengths. Then the difference of absorption cross of on-line and off-line wavelengths which was used in the following analysis could be obtained by Equation (4).

The Gaussian noise was added to the simulated echo signal, and the echo signals of LIDAR with different SNRs are shown in Figures 6 and 7.

In the simulation analysis of different SNRs, the errors of DAOD of on-line and off-line wavelengths were caused by the noises, including the background noise, thermal noise, and so on. The DAODs of LIDAR with different SNRs are shown in the Figures 8 and 9, corresponding to the SNR of 80, 50, 30 and 10.

The integrated concentration of CO<sub>2</sub> in the range of 5 km was calculated by the inversion formula and compared with the initial concentration of CO<sub>2</sub> to obtain the inversion accuracy of CO<sub>2</sub> in different noise levels by DW-DIAL. In order to avoid the occasionality of one experiment, a total of 100 simulated experiments was performed and the mean value was considered as the inversion value for each SNR. The inversion results of different SNRs by DW-DIAL are listed in the Table 5.

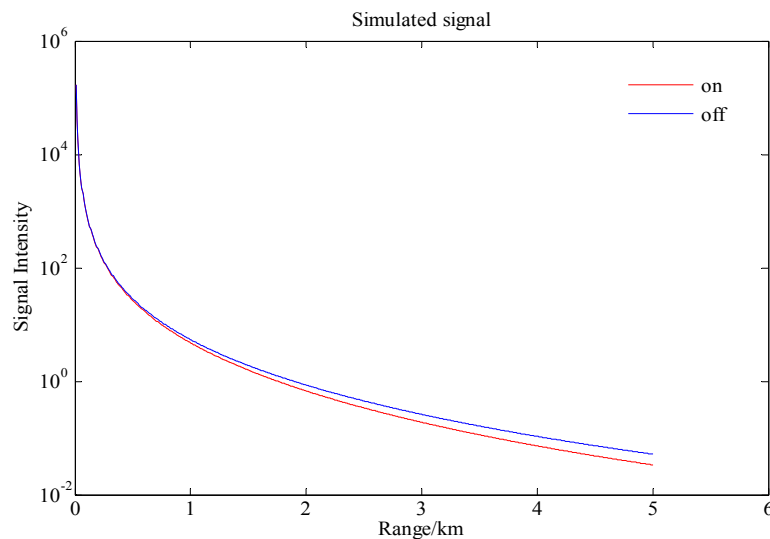


**Figure 5.** Simulated echo signal of DW-DIAL.

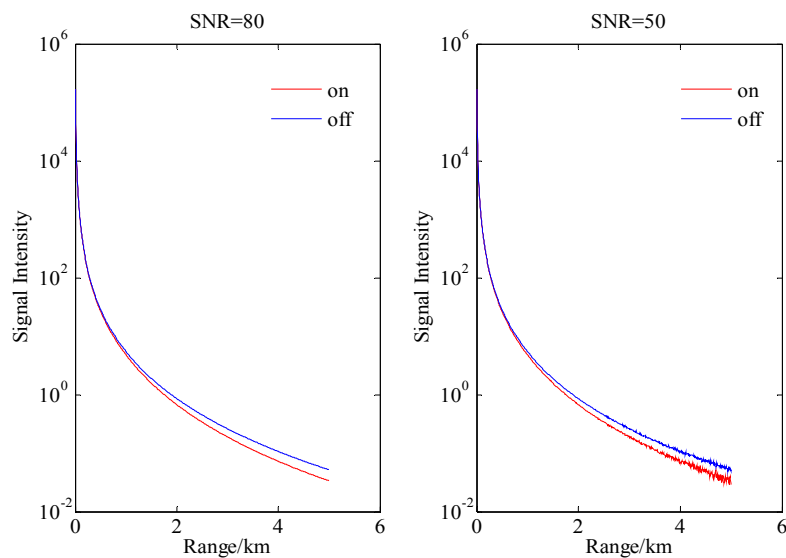


**Figure 6.** Simulated echo signal of DW-DIAL with signal to noise ratio (SNR) of 80 and 50.

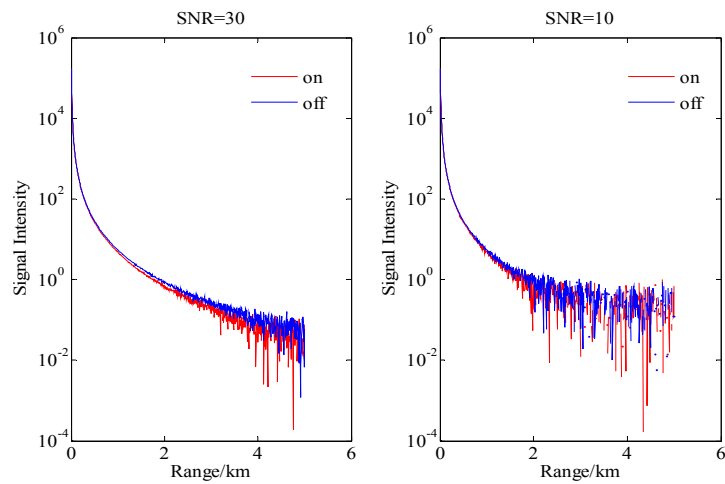


**Figure 7.** Simulated echo signal of DW-DIAL with SNR of 30 and 10.

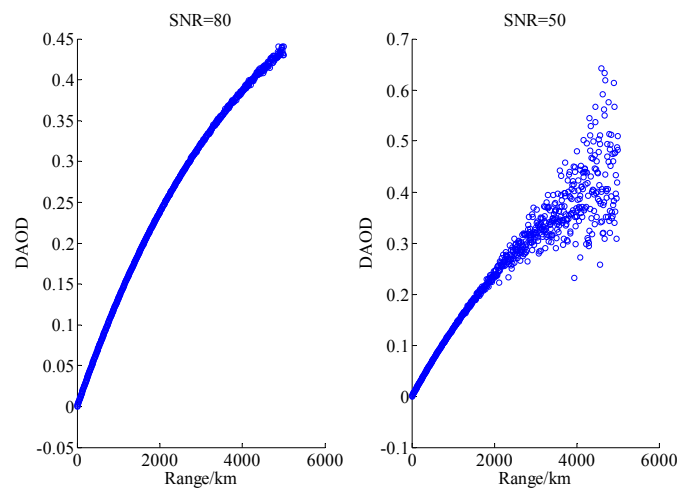


**Figure 8.** Differential absorption optical depth (DAOD) of DW-DIAL with SNR of 80 and 50.

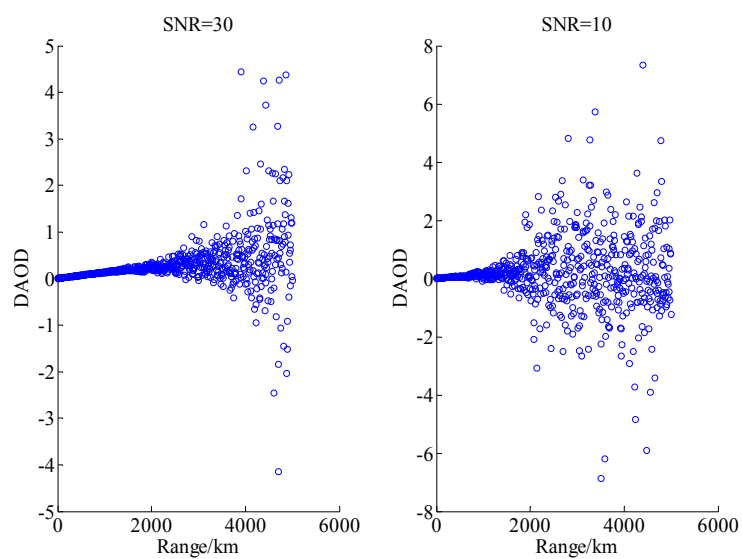


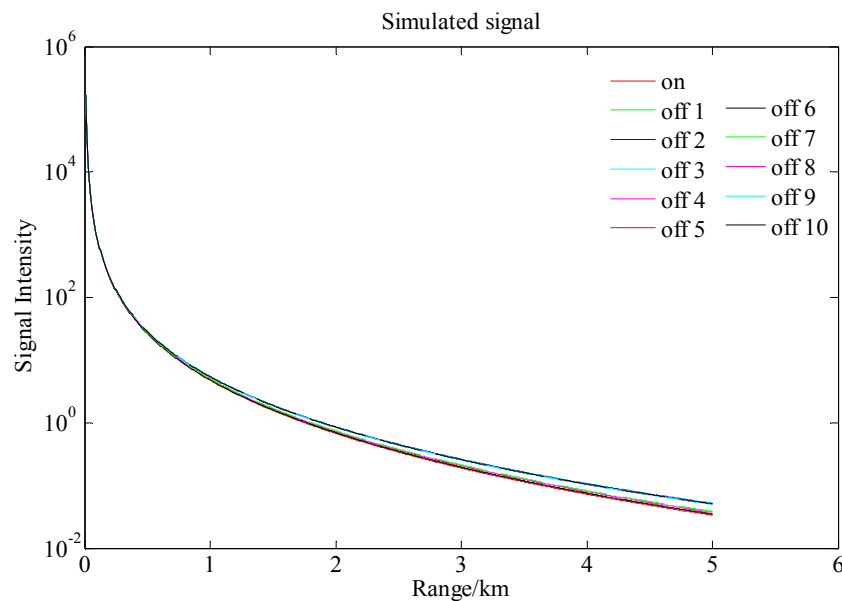
**Figure 9.** DAOD of DW-DIAL with SNRs of 30 and 10.

**Table 5.** The inversion results of different SNRs by DW-DIAL (unit: ppm).

	SNR = 80	SNR = 60	SNR = 30	SNR = 10
C	398.9184	395.5462	417.2130	34.3637

#### 4.2.2. Part 2

For the MW-DIAL, the process of simulated analysis is similar to that of DW-DIAL. The simulated signal of MW-DIAL is shown in Figure 10. To obtain the echo signals of LIDAR with different SNRs, the Gaussian noise was added. Considering the existence of 11 wavelengths, echo signals with different SNRs were not shown in this part, while the final inversion results are shown in Table 6.

**Figure 10.** Simulated echo signal of MW-DIAL.

The integrated concentration of CO<sub>2</sub> in the range of 5 km was calculated by the inversion formula and compared with the initial concentration of CO<sub>2</sub> to obtain the inversion accuracy of CO<sub>2</sub> in different noise levels by MW-DIAL. Similarly, in order to avoid the occasionality of one experiment, a total of 100 simulated experiments was performed and the mean value was considered as the inversion value for each SNR. The inversion results are shown in Table 6: C1–C10 are the inversion results of on-line wavelength and each off-line wavelength, respectively; C is the final inversion result by MW-DIAL.

**Table 6.** The inversion results of different SNRs by MW-DIAL (unit: ppm).

	SNR = 80	SNR = 60	SNR = 30	SNR = 10
C1	400.2770	399.4180	424.4756	−79.7033
C2	399.8802	398.1945	419.0777	217.3927
C3	399.9982	398.2993	422.2781	166.8717
C4	399.3138	391.1946	384.7474	291.2483
C5	399.0247	405.1858	418.5221	179.0400
C6	401.2253	401.0512	419.3369	138.6330
C7	400.3320	399.7971	427.6594	−135.2407
C8	399.9275	396.4240	383.7268	267.6911
C9	400.3947	386.4913	388.8763	210.3033
C10	400.1776	403.4622	397.0623	88.2754
C	400.1068	396.9957	406.1931	139.2494

The concentration of CO<sub>2</sub> obtained by the two methods and the difference with initial concentration (d-C for short) are listed in the Table 7. It can be noted that the inversion accuracy of MW-DIAL was better than that of DW-DIAL, especially for the signal with low SNR. In addition, there was an unacceptable inversion error for both methods while the SNR was lower than 30, thus it is necessary to eliminate the noise in the signal processing.

**Table 7.** Comparison of the inversion results by DW-DIAL and MW-DIAL (unit: ppm).

		SNR = 80	SNR = 60	SNR = 30	SNR = 10
C	DW-DIAL	398.9184	395.5462	417.2130	34.3637
	MW-DIAL	400.1068	396.9957	406.1931	139.2494
d-C	DW-DIAL	1.0816	4.4538	17.2130	365.6363
	MW-DIAL	0.1068	3.0043	6.1931	260.7506

## 5. Experiments with Laboratory Signal

Considering that our instruments did not have the capability of multi-wavelength atmospheric sounding because of the slow wavelength conversion speed at this stage, experiments through a gas absorption cell with a range of 16 m were conducted to test the feasibility and accuracy of the inversion algorithm. CO<sub>2</sub> with a purity of 100% was filled into the gas absorption cell, and the concentration of CO<sub>2</sub> was used as the evaluation standard for inversion. The temperature and pressure of the gas absorption cell was 323 K and 1 atm, respectively. Lasers with different wavelengths were coupled through the optical fiber. The OD was obtained using a high-precision sampling oscilloscope and the LabVIEW program. The concentration of CO<sub>2</sub> was calculated through the inversion algorithm with DAOD and absorption cross section from HITRAN 2012 in the laboratory experiments.

The process was similar to the simulation experiments. In the simulation experiments, DAODs were obtained by the concentration and absorption cross section from HITRAN 2012. Wavelength drifts were then added to the inversion to calculate the concentration of CO<sub>2</sub>. The inversion accuracy was evaluated by comparing the calculated value with the truth concentration. In the laboratory experiments, DAODs of different wavelengths were obtained by the gas absorption cell and high-precision sampling oscilloscope. The concentration was then calculated with DAODs and absorption cross section from HITRAN 2012. The inversion accuracy was evaluated by comparing the calculated value with the real concentration of CO<sub>2</sub> in the gas absorption cell. Wavelength drift always exists in laboratory experiments, which can be monitored using a high-precision wavemeter.

In this study, LIDAR signal was normalized by a dual-differential method using two absorption cells. The system configuration of the wavelength control unit is shown in Figure 11. Eight percent of the pulsed laser lights transmitted from the laser system was used as the laser source of the wavelength control unit. The laser was then tapped to 90:10 using a one-sided antireflection-coated glass, which is marked as M1 in Figure 11. The lights of the 10% were transmitted to a wavemeter as part of the laser source of coarse calibration, and those of the remaining 90% were split by half using a half-reflector, which is marked as M2. Two identical laser lights were then transmitted to the 16-m absorption cells: one was filled with pure CO<sub>2</sub> and the other was a vacuum. Both lights transmitted through the 16-m absorption cell were detected by an infrared detector, and the laser intensity was collected by an oscilloscope, in which the trigger signal derived from the laser system. The connecting lines marked as 1, 2, and 4 in Figure 11 are bayonet nut connectors, whereas those marked as 3, 5, and 6 are commercial cables. The absorption line of CO<sub>2</sub> could be obtained through the ratio of the intensity of the laser of the two branches.

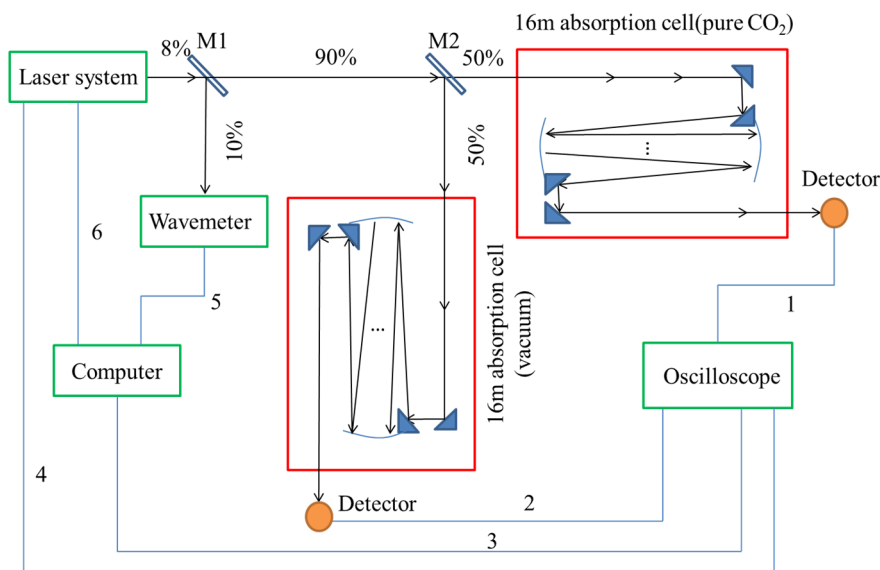


**Figure 11.** System configuration of the wavelength control unit.

In the laboratory experiments of DW-DIAL, the absorption spectra of CO<sub>2</sub> was first obtained using a gas cell with a large scale of approximately 10 m, and the absorption spectra of CO<sub>2</sub> at the region of R16 was located using a wavemeter whose accuracy was approximately 5 pm. After locating R16, we conducted a fine scanning at a step size of 3 pm and obtained the location of the on-line wavelength using a wavelength stabilization program, about which a detailed introduction is in [25]. The laser of the on-line wavelength was then imported into the gas absorption cell of the 16-m range, and the OD was obtained using the oscilloscope, following the collection procedures. The location of the off-line wavelength was determined by means of  $\lambda_{\text{off}} = \lambda_{\text{on}} - 0.1599 \text{ um}$ , which confirms with the distance between the on-line and off-line wavelengths from HITRAN 2012. The laser of the off-line wavelength was then imported to the gas absorption cell of the 16-m range, and the OD was obtained. Finally, the DAOD of the on-line and off-line wavelengths and their absorption cross section at the region of R16 from HITRAN 2012 were inserted into the inversion equation. Thus, the concentration of CO<sub>2</sub> in the gas absorption cell could be calculated. Here, the calibration of the bandwidth [33] must be the focus of attention.

In the laboratory experiments of MW-DIAL, the absorption spectra of CO<sub>2</sub> was first obtained using a gas cell with a large scale, and the absorption spectra of CO<sub>2</sub> at the region of R16 was located using a wavemeter. After locating R16, we selected 11 points according to the general principle of multiple point selection. The laser of different wavelengths was then imported into the gas absorption cell of the 16-m range, and the ODs were obtained using the oscilloscope, following the collection procedures. Finally, the DAODs of the on-line and off-line wavelengths and their absorption cross section at the region of R16 from HITRAN 2012 were plugged into the inversion equation. Accordingly, the concentration of CO<sub>2</sub> in the gas absorption cell was obtained.

Finally, the concentration of CO<sub>2</sub> in the gas absorption cell and the concentration of CO<sub>2</sub> detected through the DW-DIAL and MW-DIAL were compared to evaluate the inversion precision of the two methods. The ODs of different wavelengths and inversion results are shown in Table 8.

Table 8 reveals that the detection accuracy of CO<sub>2</sub> through MW-DIAL is higher than that through DW-DIAL, given that the wavelengths of the laser were drifting.

**Table 8.** Optical depths of different wavelengths and inversion results using the two methods.

Method	Point	OD	DAOD	$\sigma$ (cm <sup>2</sup> )	C (%)
DW-DIAL	on	1.4686	0.8193	$7.1785 \times 10^{-23}$	108.0469
	off	0.6493		$2.2250 \times 10^{-24}$	
MW-DIAL	on	1.4686	0.8193	$7.1785 \times 10^{-23}$	$C_i$ ( $i = 1, 2, \dots, 10$ ) $\frac{B_1^2 C_1 + B_2^2 C_2 + \dots + B_{10}^2 C_{10}}{B_1^2 + B_2^2 + \dots + B_{10}^2} = 98.4796$
	off_1	0.4836		$4.0309 \times 10^{-24}$	
	off_2	0.4877		$2.2087 \times 10^{-24}$	
	off_3	0.8247		$6.3319 \times 10^{-24}$	
	off_4	1.2191		$5.0866 \times 10^{-23}$	
	off_5	1.3704		$6.3286 \times 10^{-23}$	
	off_6	1.4268		$6.2279 \times 10^{-23}$	
	off_7	1.1633		$4.1391 \times 10^{-23}$	
	off_8	0.8680		$4.3222 \times 10^{-24}$	
	off_9	0.7486		$2.3463 \times 10^{-24}$	
	off_10	1.0231		$3.9719 \times 10^{-24}$	

## 6. Conclusions

In this study, an MW-DIAL was proposed for accurate detection of atmospheric CO<sub>2</sub> using a pulsed laser. The method conducts the inversion with one on-line and multiple off-line wavelengths. A feasibility study of MW-DIAL for CO<sub>2</sub> monitoring from the inversion algorithm was analyzed. The least square method was used to optimize inversion results and the inversion concentration of CO<sub>2</sub> in the MW-DIAL system was found to be the weighted average of the multiple concentrations. In addition, the single on-line and multiple off-line wavelengths were obtained through multi-wavelength scanning, which involves continuous sampling across the CO<sub>2</sub> absorption line with an appropriate number of points and range of widths. The complete absorption line of CO<sub>2</sub>, including the absorption peak and valley, could be obtained through curve fitting. This method avoids the strict locking of the on-line wavelength and therefore improves the precision of CO<sub>2</sub> detection.

Simulation analysis and laboratory experiments were conducted to evaluate the inversion precision of the two methods. The simulation analysis of wavelength drift demonstrated that—given the drifting wavelengths of the laser—the detection accuracy of CO<sub>2</sub> through MW-DIAL was higher than that through DW-DIAL, especially when the drift was large. In addition, simulated experiments indicated that wavelength stabilization is necessary in both DW-DIAL and MW-DIAL systems. However, the requirements of wavelength stabilization are more relaxed in an MW-DIAL system, which results in a more accurate detection of CO<sub>2</sub>. In the simulation analysis of different SNRs, the inversion accuracy of MW-DIAL was better than that of DW-DIAL, especially for the signal with low SNRs. A laboratory measurement was also performed to verify our simulation analysis. The errors of inversion results in a gas absorption cell were 8.0469% and 1.5204% through DW-DIAL and MW-DIAL, respectively.

The method of MW-DIAL compensates for the deficiency of stringent wavelength accuracy and stability required in a DW-DIAL system. In addition, MW-DIAL can also reduce the errors affected by other factors, such as atmospheric temperature, pressure, and the baseline variation of wavelengths.

Although the MW-DIAL has obvious advantages such as high precision and relaxed requirements of wavelength stabilization, the requirements of hardware and the receiving system are high, and the occupied space and cost are more than those of DW-DIAL. Directions for future research on MW-DIAL include the miniaturization of the laser transmitter and the development of a receiving system. In addition, in the real experiments of CO<sub>2</sub>, some errors may arise because of real atmospheric situations occurring under varying meteorological conditions.

**Acknowledgments:** This work was supported by the National Nature Science Foundation of China (No. 41127901) and the Program for Innovative Research Team in University of Ministry of Education of China (No. IRT1278). In addition, thanks to the great contribution of Xin Ma to the article.



**Author Contributions:** The study was completed with cooperation between all authors. Wei Gong and Chengzhi Xiang designed the research topic; Xin Ma, Chengzhi Xiang and FaYan conducted the experiment; Ailin Liang and Ge Han checked and analyzed the experimental results; Xin Ma and Chengzhi Xiang wrote the paper. All authors agreed with the submission of the manuscript.

**Conflicts of Interest:** The authors declare no conflicts of interest.

## References

1. Peiser, D.B. Climate change 2014. *Environ. Policy Collect.* **2014**, *27*, 408–410.
2. Salawitch, R. The human influence on global warming: Sensitivity to AMOC and OHE. In Proceedings of the 2015 AGU Fall Meeting, San Francisco, CA, USA, 14–18 December 2015.
3. Barros, V.; Field, C.; Dokke, D.; Mastrandrea, M.; Mach, K.; Bilir, T.; Chatterjee, M.; Ebi, K.; Estrada, Y.; Genova, R. Climate change 2014: Impacts, adaptation, and vulnerability. Part B: Regional aspects. In *Contribution of Working Group II to the Fifth Assessment Report of the Intergovernmental Panel on Climate Change*; IPCC: Stanford, CA, USA, 2015.
4. Williamson, R. *Global CO<sub>2</sub> Concentrations Pass 400 ppm Milestone*; Future Sci Ltd., United House: London, UK, 2013.
5. Idso, C.D.; Idso, S.B.; Balling, R.C. An intensive two-week study of an urban CO<sub>2</sub> dome in Phoenix, Arizona, USA. *Atmos. Environ.* **2001**, *35*, 995–1000. [[CrossRef](#)]
6. Cox, P.M.; Betts, R.A.; Jones, C.D.; Spall, S.A.; Totterdell, I.J. Acceleration of global warming due to carbon-cycle feedbacks in a coupled climate model. *Nature* **2000**, *408*, 184–187. [[CrossRef](#)] [[PubMed](#)]
7. Friedlingstein, P.; Cox, P.; Betts, R.; Bopp, L.; Von Bloh, W.; Brovkin, V.; Cadule, P.; Doney, S.; Eby, M.; Fung, I. Climate-carbon cycle feedback analysis: Results from the c4mip model intercomparison. *J. Clim.* **2006**, *19*, 3337–3353. [[CrossRef](#)]
8. Lac, C.; Donnelly, R.; Masson, V.; Pal, S.; Donier, S.; Queguiner, S.; Tanguy, G.; Ammoura, L.; Xueref-Remy, I. CO<sub>2</sub> dispersion modelling over paris region within the CO<sub>2</sub>-megaparis project. *Atmos. Chem. Phys.* **2013**, *13*, 4941–4961. [[CrossRef](#)]
9. Pal, S.; Xueref-Remy, I.; Ammoura, L.; Chazette, P.; Gibert, F.; Royer, P.; Dieudonné, E.; Dupont, J.-C.; Haeffelin, M.; Lac, C. Spatio-temporal variability of the atmospheric boundary layer depth over the paris agglomeration: An assessment of the impact of the urban heat island intensity. *Atmos. Environ.* **2012**, *63*, 261–275. [[CrossRef](#)]
10. Fiorani, L.; Santoro, S.; Parracino, S.; Nuvoli, M.; Minopoli, C.; Aiuppa, A. Volcanic CO<sub>2</sub> detection with a DFM/OPA-based LIDAR. *Opt. Lett.* **2015**, *40*, 1034–1036. [[CrossRef](#)] [[PubMed](#)]
11. Fix, A.; Büdenbender, C.; Wirth, M.; Quatrevalet, M.; Amediek, A.; Kiemle, C.; Ehret, G. Optical parametric oscillators and amplifiers for airborne and spaceborne active remote sensing of CO<sub>2</sub> and CH<sub>4</sub>. *Proc. SPIE* **2011**, *818*, 206–210.
12. Gibert, F.; Flamant, P.H.; Bruneau, D.; Loth, C. Two-micrometer heterodyne differential absorption LIDAR measurements of the atmospheric CO<sub>2</sub> mixing ratio in the boundary layer. *Appl. Opt.* **2006**, *45*, 4448–4458. [[CrossRef](#)] [[PubMed](#)]
13. Singh, U.N.; Yu, J.; Petros, M.; Refaat, T.; Reithmaier, K. Development of a pulsed 2-micron integrated path differential absorption LIDAR for CO<sub>2</sub> measurement. *Proc. SPIE* **2013**. [[CrossRef](#)]
14. Abshire, J.B.; Riris, H.; Allan, G.R.; Weaver, C.J.; Mao, J.; Sun, X.; Hasselbrack, W.E.; Yu, A.; Amediek, A.; Choi, Y. A LIDAR approach to measure CO<sub>2</sub> concentrations from space for the ascends mission. In Proceedings of the Remote Sensing International Society for Optics and Photonics, Vienna, Austria, 2–7 May 2010.
15. Refaat, T.F.; Singh, U.N.; Yu, J.; Petros, M.; Ismail, S.; Kavaya, M.J.; Davis, K.J. Evaluation of an airborne triple-pulsed 2 µm IPDA LIDAR for simultaneous and independent atmospheric water vapor and carbon dioxide measurements. *Appl. Opt.* **2015**, *54*, 1387–1398. [[CrossRef](#)] [[PubMed](#)]
16. Abshire, J.B.; Ramanathan, A.; Riris, H.; Mao, J.; Allan, G.R.; Hasselbrack, W.E.; Weaver, C.J.; Browell, E.V. Airborne measurements of CO<sub>2</sub> column concentration and range using a pulsed direct-detection IPDA LIDAR. *Remote Sens.* **2013**, *6*, 443–469. [[CrossRef](#)]
17. Behrendt, A.; Wagner, G.; Petrova, A.; Shiler, M.; Pal, S.; Schaberl, T.; Wulfmeyer, V. Modular LIDAR systems for high-resolution 4-dimensional measurements of water vapor, temperature, and aerosols. *Proc. SPIE* **2005**. [[CrossRef](#)]

18. Behrendt, A.; Wulfmeyer, V.; Riede, A.; Wagner, G.; Pal, S.; Bauer, H.; Radlach, M.; Späth, F. Three-dimensional observations of atmospheric humidity with a scanning differential absorption LIDAR. *Proc. SPIE* **2009**. [CrossRef]
19. Amediek, A.; Fix, A.; Ehret, G.; Caron, J.; Durand, Y. Airborne LIDAR reflectance measurements at 1.57  $\mu\text{m}$  in support of the a-scope mission for atmospheric  $\text{CO}_2$ . *Atmos. Meas. Tech.* **2009**, *2*, 755–772. [CrossRef]
20. Schotlan, R.M. Errors in the LIDAR measurement of atmospheric gases by differential absorption. *J. Appl. Meteorol.* **1974**, *13*, 71–77.
21. Gong, W.; Han, G.; Ma, X.; Lin, H. Multi-points scanning method for wavelength locking in  $\text{CO}_2$  differential absorption LIDAR. *Opt. Commun.* **2013**, *305*, 180–184. [CrossRef]
22. Gong, W.; Ma, X.; Dong, Y.; Lin, H.; Li, J. The use of 1572 nm MIE LIDAR for observation of the optical properties of aerosols over Wuhan, China. *Opt. Laser Technol.* **2014**, *56*, 52–57. [CrossRef]
23. Ehret, G.; Kiemle, C.; Wirth, M.; Amediek, A.; Fix, A.; Houweling, S. Space-borne remote sensing of  $\text{CO}_2$ ,  $\text{CH}_4$ , and  $\text{N}_2\text{O}$  by integrated path differential absorption LIDAR: A sensitivity analysis. *Appl. Phys. B* **2008**, *90*, 593–608. [CrossRef]
24. Abshire, J.B.; Riris, H.; Allan, G.R.; Weaver, C.J.; Mao, J.; Sun, X.; Hasselbrack, W.E.; Kawa, S.R.; Biraud, S. Pulsed airborne LIDAR measurements of atmospheric  $\text{CO}_2$  column absorption. *Tellus B* **2010**, *62*, 770–783. [CrossRef]
25. Han, G.; Gong, W.; Lin, H.; Ma, X.; Xiang, C. On-line wavelength calibration of pulsed laser for  $\text{CO}_2$  DIAL sensing. *Appl. Phys. B* **2014**, *117*, 1041–1053. [CrossRef]
26. Gong, Z.-W. Least-square method to priority of the fuzzy preference relations with incomplete information. *Int. J. Approx. Reason.* **2008**, *47*, 258–264. [CrossRef]
27. Lukas, H.; Henig, E.T.; Zimmermann, B. Optimization of phase diagrams by a least squares method using simultaneously different types of data. *Calphad* **1977**, *1*, 225–236. [CrossRef]
28. Predoi-Cross, A.; McKellar, A.; Benner, D.C.; Devi, V.M.; Gamache, R.; Miller, C.; Toth, R.; Brown, L. Temperature dependences for air-broadened lorentz half-width and pressure shift coefficients in the 30013←00001 and 30012←00001 bands of  $\text{CO}_2$  near 1600 nm this article is part of a special issue on spectroscopy at the university of new brunswick in honour of colan linton and ron lees. *Can. J. Phys.* **2009**, *87*, 517–535.
29. Rothman, L.; Gordon, I.; Babikov, Y.; Barbe, A.; Benner, D.C.; Bernath, P.; Birk, M.; Bizzocchi, L.; Boudon, V.; Brown, L. The HITRAN 2012 molecular spectroscopic database. *J. Quant. Spectrosc. Radiat. Transf.* **2013**, *130*, 4–50. [CrossRef]
30. Rothman, L.; Gordon, I.; Barber, R.; Dothe, H.; Gamache, R.; Goldman, A.; Perevalov, V.; Tashkun, S.; Tennyson, J. HITEMP, the high-temperature molecular spectroscopic database. *J. Quant. Spectrosc. Radiat. Transf.* **2010**, *111*, 2139–2150. [CrossRef]
31. Han, G.; Lin, H.; Ma, X.; Xiang, Z. Study on influences of atmospheric factors on vertical  $\text{CO}_2$  profile retrieving from ground-based dial at 1.6  $\mu\text{m}$ . *IEEE Trans. Geosci. Remote Sens.* **2014**. [CrossRef]
32. Amediek, A.; Fix, A.; Wirth, M.; Ehret, G. Development of an opo system at 1.57  $\mu\text{m}$  for integrated path dial measurement of atmospheric carbon dioxide. *Appl. Phys. B* **2008**, *92*, 295–302. [CrossRef]
33. Han, G.; Gong, W.; Ma, X.; Xiang, C.-Z.; Liang, A.-L.; Zheng, Y.-X. A ground-based differential absorption LIDAR for atmospheric vertical  $\text{CO}_2$  profiling. *Acta Phys. Sin.* **2015**, *64*. [CrossRef]

